ChemPubSoc Europe

DOI: 10.1002/chem.201504140

CHEMISTRY A European Journal Full Paper

Ion–Molecule Reactions

Capturing Transient Endoperoxide in the Singlet Oxygen Oxidation of Guanine

Wenchao Lu and Jianbo Liu*[a]

Abstract: The chemistry of singlet O_2 toward the guanine base of DNA is highly relevant to DNA lesion, mutation, cell death, and pathological conditions. This oxidative damage is initiated by the formation of a transient endoperoxide through the Diels–Alder cycloaddition of singlet O_2 to the guanine imidazole ring. However, no endoperoxide formation was directly detected in native guanine or guanosine, even at −100 °C. Herein, gas-phase ion–molecule scattering mass spectrometry was utilized to capture unstable endoperoxides in the collisions of hydrated guanine ions (protonated or deprotonated) with singlet O_2 at ambient temperature. Corroborated by results from potential energy surface exploration, kinetic modeling, and dynamics simulations, various aspects of endoperoxide formation and transformation (including its dependence on guanine ionization and hydration states, as well as on collision energy) were determined. This work has pieced together reaction mechanisms, kinetics, and dynamics data concerning the early stage of singlet O_2 induced guanine oxidation, which is missing from conventional condensed-phase studies.

Introduction

DNA of living systems is constantly exposed to endo- and exogenously generated reactive oxygen species.[1] Of the four DNA nucleobases, electronically excited singlet oxygen ($^1O_2$) oxidizes guanine exclusively.[2] Oxidation of guanine in isolated nucleosides and short oligonucleotides gives rise to spiroiminodihydantoin (Sp) and guanidinohydantoin (Gh);[2g] whereas the guanine moiety in isolated and cellular DNA is mainly oxidized to 8-oxo-7,8-dihydroguanine (8-oxoG).[2m] The consequences of $^1O_2$-induced primary and secondary oxidative lesions of guanine[2h,k,m,3] are implicated in photocleavage, mutagenesis, carcinogenesis, and cell death.[4] By mispairing with adenine during replication, 8-oxoG gives rise to G·C→T·A transversion—a somatic mutation in cancers.[5] Sp and Gh are even more mutagenic, leading to G to C and G to T transversions.[6] The formation of 8-oxoG is also related to neurological disorders responsible for Alzheimer's and Parkinson's diseases,[7] and triggers DNA–protein cross-links.[8]

Much mechanistic work on guanine oxidation was carried out by using photosensitized $^1O_2$[9] oxidation of oligonucleotides and isolated[2q]/cellular[2c] DNA in the presence of dyes and light (or naphthalene endoperoxide, which released $^1O_2$[10]). It has been assumed that an endoperoxide is the initial intermediate, leading to the formation of final oxidation products of guanine. However, the verification of endoperoxide formation is not straightforward because of the instability of the endoperoxide and its reactivity with water.[2a,11] So far, the only information on this mechanism was extrapolated from trapping and NMR spectroscopic characterization of an endoperoxide formed in the photo-oxidation of 2′,3′,5′-*O*-(*tert*-butyldimethylsilyl)-8-methylguanosine at −78 °C, presumably because substitution of the labile C8-H of guanine with an alkyl group stabilized the endoperoxide. When warmed to −30 °C, 8-methylguanosine endoperoxide decomposed back to starting reactants through a retro-Diels–Alder reaction.[2a] Attempts to detect endoperoxide formation in native and other guanosine derivatives failed, even down to −100 °C.[11]

The purpose of this work was to investigate $^1O_2$ chemistry with guanine in the gas phase. We used isolated protonated ($[G+H]^+$) and deprotonated ($[G-H]^-$) guanine as targets, and probed their reactions with "clean" $^1O_2$ produced through the reaction of H_2O_2 and Cl_2 in basic solution[12] without the formation of radical byproducts. Transient endoperoxides were formed in the collisions of guanine ions with $^1O_2$ at ambient temperature, and detected directly by a guided-ion-beam tandem mass spectrometer. Different aspects of endoperoxide formation were examined, including its dependence on collision energy (E_{col}), and guanine ionization and hydration states. Experimental results were corroborated by kinetic modeling and dynamics simulations, leading to new insights into the early stage of the reaction of $^1O_2$ with guanine, with a focus on the formation and transformation of oxidation intermediates. This work has exemplified that gas-phase ion–molecule reactions[13] are able to probe the intrinsic reactivity of DNA bases[14] and the effect of an explicit water ligand.

[a] *W. Lu, Prof. J. Liu*
Department of Chemistry and Biochemistry
Queens College and the Graduate Center
of the City University of New York
65-30 Kissena Blvd, Queens, NY 11367 (USA)
E-mail: jianbo.liu@qc.cuny.edu

Supporting information and ORCID(s) from the author(s) for this article are available on the WWW under http://dx.doi.org/10.1002/chem.201504140.

Results and Discussion

1. Structures of gas-phase guanine in different ionization and hydration states

Guanine has keto–enol and N9H–N7H tautomerization.[15] As illustrated in Figure 1, the 7H-keto tautomer, with the H atoms positioned at N1 and N7, represents the global minimum, whereas the 9H-ketone, with H atoms at N1 and N9, represents the second lowest lying tautomer. Based on B3LYP/aug-cc-pVQZ//B3LYP/6-311++G** calculations, the 7H- and 9H-ketones represent 69 and 24% of the guanine population at 298 K, respectively. The remaining population is shared by three enol tautomers. All of these tautomers were detected by gas-phase spectroscopy.[15a–e]

Twenty-nine tautomers were identified for $[G+H]^+$ (as summarized in Figure S1 in the Supporting Information), involving O, C, and different N sites as proton acceptors and presenting large energy differences. Four low-energy tautomers lie within 0.2 eV (see Figure 1), including keto–amino tautomers ($[G+H]^+$_1 with a population of 90.6%, and $[G+H]^+$_4, <0.1% population) and enol–amino tautomers ($[G+H]^+$_2, 8.9%, and $[G+H]^+$_3, 0.4%). The most stable tautomer is formed by protonation of the N9 of the 7H-ketone (or N7 of the 9H-ketone).[15f,g,j,16] The B3LYP/aug-cc-pVQZ-calculated proton affinity of the 7H-ketone is 964 kJ mol^{-1}, which is in agreement with the experimental values of (951±48)[17] and 959.5 kJ mol^{-1}.[18]

We found 15 tautomers for $[G-H]^-$, including deprotonation of N1, the imidazole N, and the amino group[19] of neutral tautomers. The C8 site is much less acidic than those of the N sites and was excluded.[19b] The structures of $[G-H]^-$ are presented in Figure S2 in the Supporting Information, and those within 0.2 eV energy range are included in Figure 1. Consistent with the literature,[15j,16b,c,19b] deprotonation of N1 and N7 of the 7H-ketone leads to the two most stable deprotonated tautomers, $[G-H]^-$_1 and 2, with B3LYP/aug-cc-pVQZ-calculated 298 K populations of 75 and 15% and gas-phase acidities (GPA) of 1384 and 1388 kJ mol^{-1}, respectively. For comparison, the experimental GPA value is (1389±13) kJ mol^{-1}.[19a]

The initial geometries of the monohydrated ions were obtained by adding a water molecule to the $[G+H]^+$ and $[G-H]^-$

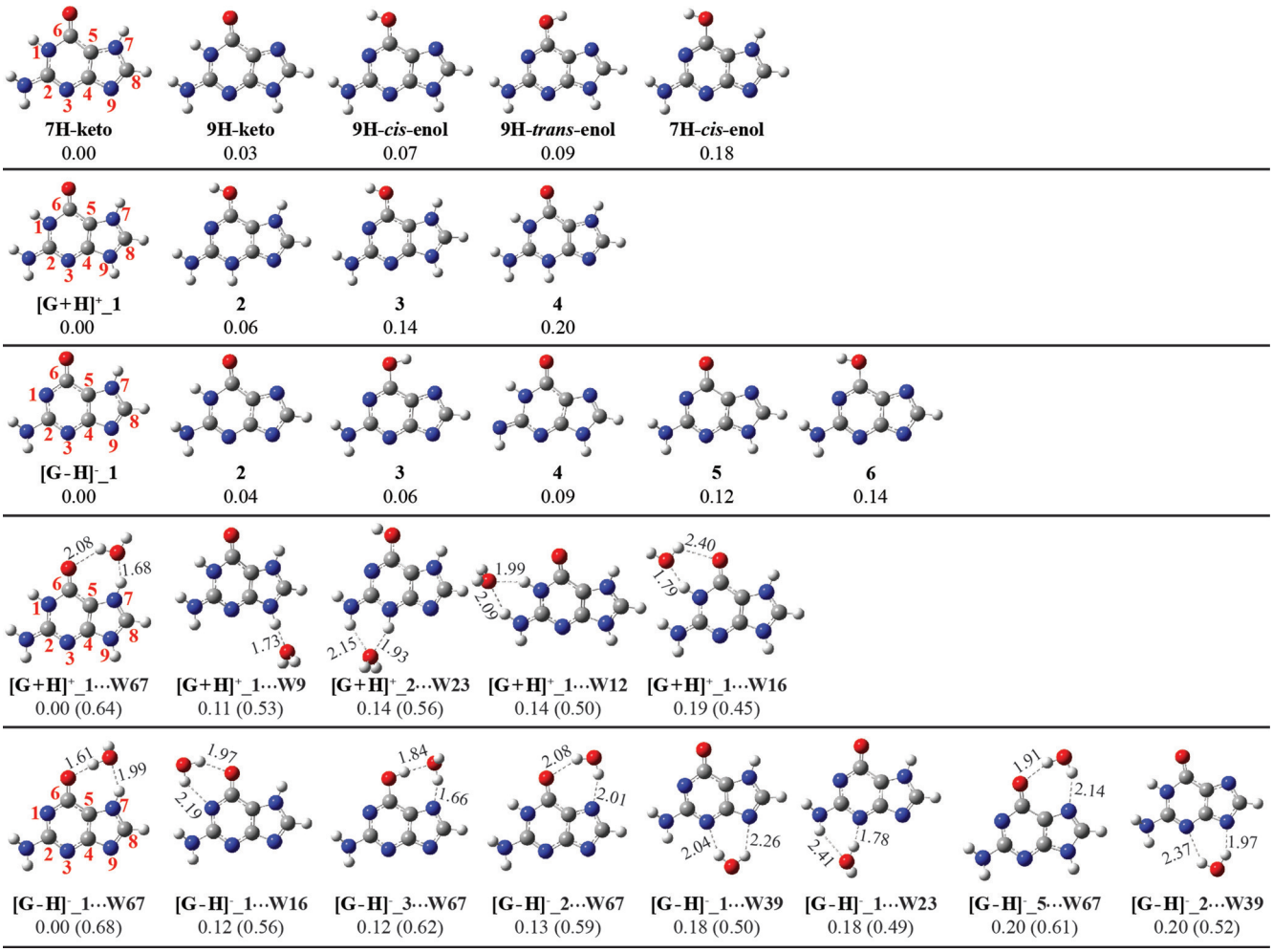

Figure 1. Low-lying tautomers of G, $[G+H]^+(H_2O)_{0,1}$, and $[G-H]^-(H_2O)_{0,1}$. The numbering scheme and nomenclature are presented. Dashed lines indicate hydrogen bonds. Bond lengths are shown in Å. Relative energies [eV] and hydration energies (presented in parentheses) were evaluated based on the sum of electronic energy calculated at the B3LYP/aug-cc-pVQZ//B3LYP/6-311++G** level with thermal correction (298 K) at the B3LYP/6-311++G** level.

tautomers in Figure 1, and then optimizing the structures at the B3LYP/6-311++G** level. Different hydrogen-bonding sites and orientations of the water ligand were considered. The converged structures are reported in Figures S3 and S4 in the Supporting Information. Most hydrates form cyclic complexes through two hydrogen bonds. Such water-binding motifs are similar to those found for neutral guanine.[15i,16b,20] The hydration energy was calculated by using Equation (1):

$$E_{\text{hydration}} = E(\text{bare ion}) + E(H_2O) - E(\text{cluster}) \quad (1)$$

in which E(bare ion), $E(H_2O)$, and E(cluster) are the energies of bare ion, water, and the hydrate of the same ion tautomer, respectively. The most stable protonated and deprotonated monohydrates are formed by a water hydrogen bonded to the carbonyl and N7H sites concurrently. They account for 98 and 97% of the protonated and deprotonated monohydrates, respectively.

On the basis of their overwhelming populations, $[G+H]^+$_1, $[G-H]^-$_1, $[G+H]^+$_1···W67 and $[G-H]^-$_1···W67 represent reactant structures in corresponding gas-phase reactions with $^1O_2$.

2. Fate of isolated guanine endoperoxide

We first examined the gas-phase reactions of $^1O_2$ with bare $[G+H]^+$ and $[G-H]^-$ over the center-of-mass E_{col} range of 0.1–1.0 eV. The experiment was performed on a guided-ion-beam tandem mass spectrometer,[21] as described in the Experimental and Computational Section. $[G+H]^+$ and $[G-H]^-$ ions were generated by electrospray ionization (ESI). To eliminate radicals and other reactive oxygen species that accompany with photosensitization of $^3O_2$, $^1O_2$ was produced from Reaction (1).[22]

$$H_2O_2 + Cl_2 + 2KOH \rightarrow {}^1O_2/{}^3O_2 + 2KCl + 2H_2O \quad (1)$$

The surprise was that all protonated/deprotonated guanine molecules survived $^1O_2$ attack. No oxidation products were detected. The only consequence of guanine–$^1O_2$ scattering was collision-induced dissociation, including elimination of NH_3 and NHCNH from $[G+H]^+$[14n,p,23] and NH_3 and HNCO from $[G-H]^-$.[14r,23,24]

Nonreactivity of $[G+H]^+$ toward $^1O_2$: To explore the origin of this nonreactivity, we have mapped out the potential energy surface (PES) associated with the reaction coordinate for $[G+H]^+ + {}^1O_2$. Intersystem crossing of $[G+H]^+ + {}^1O_2 \rightarrow {}^3[G+H]^+ + {}^3O_2$ was excluded because the threshold for this electronic excitation transfer (0.99 eV) was near the maximum experimental value of E_{col}; consequently the reaction system remained in the singlet state. Calculation results are summarized in Figure 2. B3LYP/6-31+G* was chosen for most of our calculations because this DFT method has been successfully used in probing the $^1O_2$ oxidation of 6-thioguanine,[25] the transformation of 8-oxoguanine,[26] and the [4+2] cycloaddition of $^1O_2$ onto histidine.[27] Energies of critical intermediates were refined by using single-point calculations at the CCSD(T)/6-31+G* level. To ascertain if our calculations might be invalidated by large contributions from species other than the Hartree–Fock configuration,[28] CASSCF(10,10)/6-31+G* was performed for the most critical structures, PC^+, $TS1a^+$, and 5,8-OO-$[G+H]^+$, along the cycloaddition path shown in Figure 2. In all cases, the coefficient of the Hartree–Fock configuration exceeded 0.95. We also inspected the quality of the single-reference electron correlation approach with T1 diagnostic for $TS1a^+$ and 5,8-OO-$[G+H]^+$. The T1 values derived from CCSD(T) calculations are 0.0180 and 0.020, respectively, which indicate that the static contribution to the total electron correlation can be neglected. These tests suggest that our calculations are appropriate for describing the most important part of the reaction. Notably, Grüber et al. examined the stability of the endoperoxide and 8-peroxide derivatives of neutral guanine by using various methods,[29] and found that multireference calculations were not necessary.

Two reaction pathways may be inferred from the PES in Figure 2. The first one corresponds to reactants→reactant-like precursor $PC^+ \rightarrow TS1a^+ \rightarrow$5,8-OO-$[G+H]^+ \rightarrow TS1b^+$, $TS1c^+$, and $TS1d^+ \rightarrow$5-OH-8-oxoG^+, followed by $TS1e^+$_1→8-oxo$[G-H]^+ + H_2O$ or $TS1e^+$_2→$[Sp+H]^+$. The reaction is initiated by the Diels–Alder cycloaddition of the O_2 moiety to the imidazole C5—C8 bond, leading to a protonated endoperoxide, 5,8-OO-$[G+H]^+$. We have explored the possibility of forming a 4,8-endoperoxide by running a relaxed PES scan along the approach of one O atom of O_2 toward C4. The *r*O—C4 bond length was continuously varied, and all other coordinates were optimized at each step. However, the PES avoided cycloaddition to C4—C8, but instead converged to 5,8-OO-$[G+H]^+$. The 5,8-OO-$[G+H]^+$ species may rearrange to 5-OH-8-oxoG^+ through consecutive activation barriers: the dioxo bridge breaks at $TS1b^+$, followed by intramolecular H transfer from C8 to N7 at $TS1c^+$, and then from N7 to C5-O at $TS1d^+$. The ensuing 5-OH-8-oxoG^+ species may eliminate a water, producing 8-oxo$[G-H]^+$. The reaction enthalpy (ΔH_{rxn}) for 8-oxo$[G-H]^+ + H_2O$ is −3.38 eV, but the transition states (TSs) amount to a barrier of 0.92 eV. Alternatively, 5-OH-8-oxoG^+ may rearrange to form $[Sp+H]^+$,[30] which involves migration of the C6 acyl group to C4 at $TS1e^+$_2, with $\Delta H_{rxn} = -4.06$ eV.

In the second pathway, the reactants first form an open adduct, 8-OO$[G+H]^+$, through the addition of $^1O_2$ to the C8 position.[29] However, a more energetically favorable formation path for 8-OO$[G+H]^+$ is through interconversion from 5,8-OO-$[G+H]^+$ without a backward barrier, as verified by a relaxed PES scan. The 8-OO$[G+H]^+$ species has an intramolecular zwitterionic nature, as indicated by population analysis. We were concerned that it might suffer from charge over-delocalization in the B3LYP calculation. Grüber et al. reported that some DFT methods incorrectly predicted the stability of neutral guanine endoperoxide versus its 8-peroxide.[29] Fortunately, this was not the case for our system. We used MP3/aug-cc-pVTZ//MP2/6-31+G* to benchmark the energy gap between 5,8-OO-$[G+H]^+$ and 8-OO$[G+H]^+$, which was −2.1 eV. The CCSD(T)/6-31+G*//B3LYP/6-31+G*-predicted energy gap (−1.64 eV) was comparable to this benchmark. The 8-OO$[G+H]^+$ species

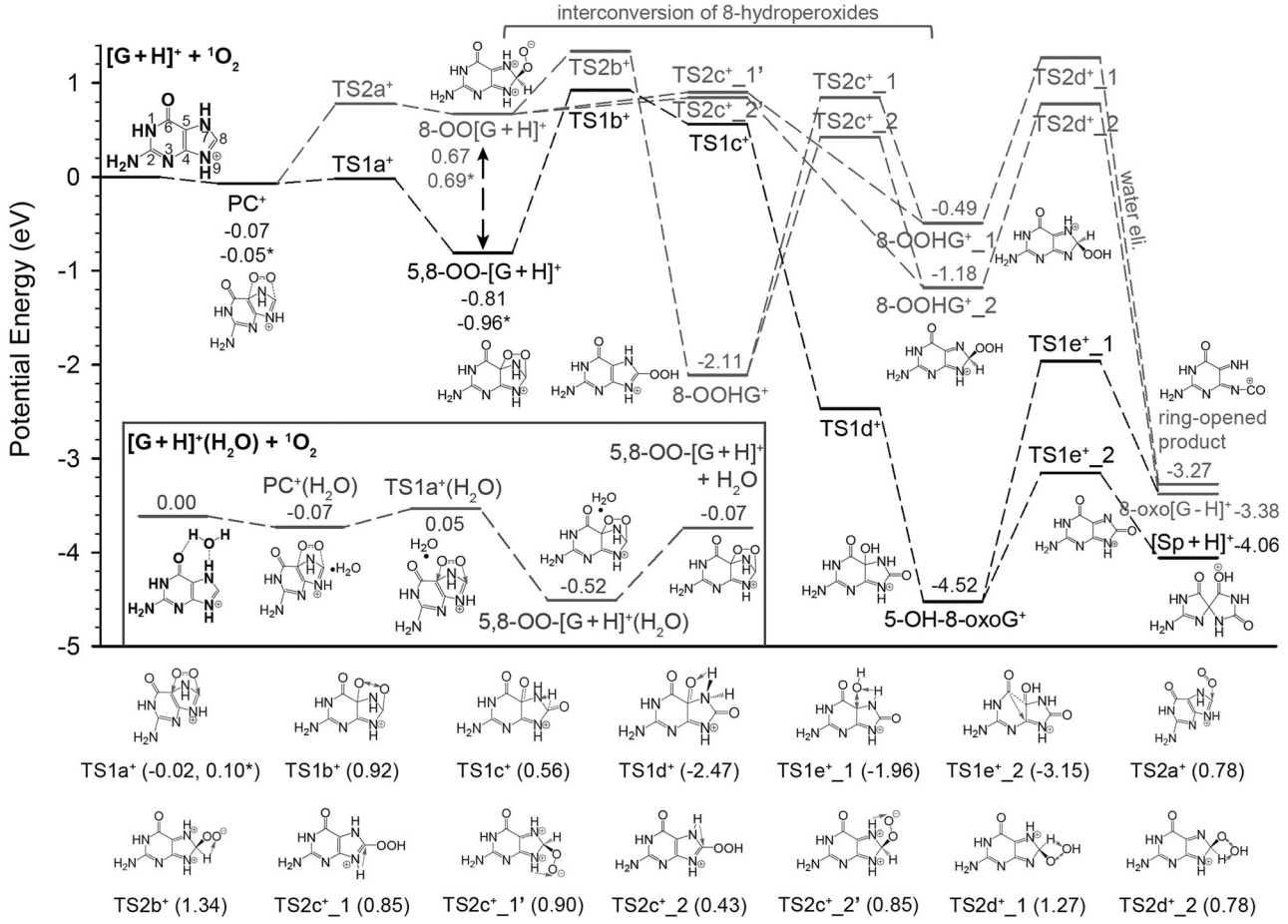

Figure 2. Reaction coordinate for $[G+H]^+ + {}^1O_2$. Inset shows the reaction coordinate for $[G+H]^+(H_2O) + {}^1O_2$, in which water evaporation prompts the formation of a stable endoperoxide. Energies (relative to reactants) were calculated at the B3LYP/6-31+G* level, including thermal corrections at 298 K. Energies of critical intermediates were refined by using single-point CCSD(T)/6-31+G* calculations, as indicated by asterisks.

interconverts to 8-$OOHG^+$ via $TS2b^+$. The latter evolves to 8-$OOHG^+$_1 and 2 via $TS2c^+$_1 and 2, respectively. The 8-$OO[G+H]^+$ species may also rearrange to 8-$OOHG^+$_1 and 2 via $TS2c^+$_1′ and 2′, respectively. The 8-$OOHG^+$, 8-$OOHG^+$_1, and 8-$OOHG^+$_2 species are all 8-hydroperoxides; the difference is which H is abstracted to form −OOH. The 8-$OOHG^+$_1 species opens the imidazole ring through dehydration, yielding pyrimidine-like cyclic-$[NHC(NH_2)NC(=NCO)C(=NH)C(=O)]^+$. The 8-$OOHG^+$_2 species eliminates a water molecule from C8, producing 8-oxo$[G-H]^+$.

However, the intermediates and products resulting from these two pathways may all be discounted at low E_{col} because of high activation barriers. The only exception is 5,8-OO-$[G+H]^+$, which has favorable energetics. However, 5,8-OO-$[G+H]^+$ was not present in the product mass spectra. The mechanistic importance of an intermediate also depends on its lifetime, so we used the Rice–Ramsperger–Kassel–Marcus (RRKM)[31] theory to calculate dissociation rates leading from 5,8-OO-$[G+H]^+$. At low E_{col}, only one dissociation channel is appreciable for 5,8-OO-$[G+H]^+$, namely, decay back to reactants. The rotational quantum number, K, was treated as active in evaluating the rate constant, $k(E, J)$, and all $(2J+1)K$-levels were counted as shown by Equation (2):[32]

$$k(E,J) = \frac{d}{h}\frac{\sum_{K=-J}^{J} G[E - E_0 - E_r^{+}(J,K)]}{\sum_{K=-J}^{J} N[E - E_r(J,K)]} \quad (2)$$

in which d is the reaction path degeneracy; G is the sum of states from 0 to $E-E_0-E_r^{\dagger}$ at $TS1a^+$; N is the reactant density of states; E is the system energy; E_0 is the dissociation threshold; and E_r and $E_r^{\dagger}$ are the rotational energies of 5,8-OO-$[G+H]^+$ and $TS1a^+$, respectively. The orbital angular momentum, L, was estimated from the collision cross section, $\sigma_{collision}$, that is, $L = \mu v_{rel}(\sigma_{collision}/\pi)^{1/2}$, in which μ and v_{rel} are the reduced mass and relative velocity of collision partners, respectively. The properties of 5,8-OO-$[G+H]^+$ and $TS1a^+$ were described by using B3LYP-calculated frequencies, polarizabilities, and moments of inertia.

The most critical kinetic insight obtained from RRKM analysis is that, at $E_{col} \leq 0.2$ eV (at which complex mediation is expected to be important), the lifetime of 5,8-OO-$[G+H]^+$ is only 30–130 μs. For comparison, the time-of-flight of product ions through the octopole and the second quadrupole of the mass spectrometer is 400–500 μs in this E_{col} range. As a result, 5,8-OO-$[G+H]^+$ was too short-lived to be detected by MS.

Influences of guanine ionization: Although both protonated and deprotonated guanine are not reactive with $^1O_2$, the guanine ionization state affects the reaction profile, particularly the reaction intermediates. The PES for the reaction of $[G-H]^-$ with $^1O_2$ is shown in Figure 3a. To facilitate a comparison of the PESs of different ionic states, the corresponding structures are assigned identical names, but with +/− superscripts to distinguish between ionization forms. Similar to the protonated system, the reaction of $[G-H]^-$ first forms an endoperoxide, 5,8-OO-$[G-H]^-$, or a peroxide, 8-OO$[G-H]^-$, two of which undergo interconversion. In contrast to 5,8-OO-$[G+H]^+$, which may break the dioxo bridge, no such pathway was found for 5,8-OO-$[G-H]^-$. The 8-OO$[G-H]^-$ species may evolve to form 8-OOH$[G-2H]^-$ and its tautomeric isomer 8-OOH$[G-2H]^-$_1; the latter undergoes water elimination to give 8-oxo$[G-3H]^-$.

Based on RRKM analysis, a kinetically favorable pathway for the deprotonated system is $[G-H]^- + {}^1O_2 \rightarrow PC^- \rightarrow TS1^- \rightarrow$ 5,8-OO-$[G-H]^- \rightarrow$8-OO$[G-H]^- \rightarrow$TS2c$^-$_1$\rightarrow$8-OOH$[G-2H]^-$_1. We calculated the rate constants leading from 8-OOH$[G-2H]^-$_1 to 8-oxo$[G-3H]^-$, back to 8-OO$[G-H]^-$, and rounding into 8-OOH$[G-2H]^-$. They were 4×10^{-5}, 3×10^{5}, and $6\times10\ s^{-1}$, respectively, at $E_{col}=0.1$ eV. It follows that 8-OOH$[G-2H]^-$_1, if formed, overwhelmingly converts back to its predecessor 8-OO$[G-H]^-$. Neither 8-oxo$[G-3H]^-$ nor 8-OOH$[G-2H]^-$ were significant. In this scenario, the total lifetime of PC1$^-$, 5,8-OO-$[G-H]^-$, 8-OO$[G-H]^-$, and 8-

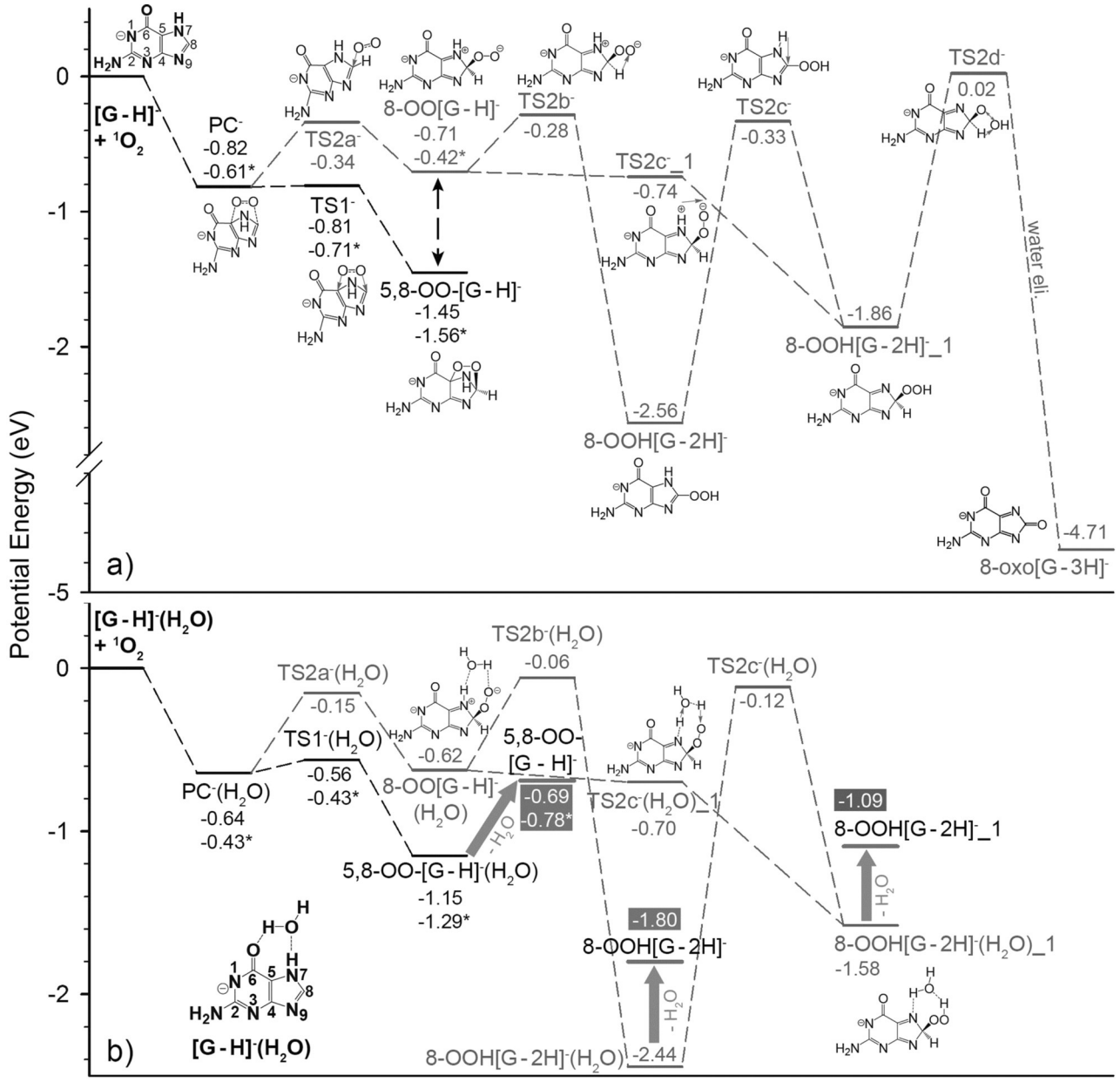

Figure 3. Reaction coordinates for a) $[G-H]^- + {}^1O_2$ and b) $[G-H]^-(H_2O) + {}^1O_2$. The geometries of hydrated species in b) are identical to their dehydrated analogues in a), except with a water attached to C6O and N7H. Energies (relative to reactants) were calculated at the B3LYP/6-31+G* level, including thermal corrections at 298 K. Energies of critical intermediates were refined by using single-point CCSD(T)/6-31+G* calculations, as indicated with asterisks.

OOH[G−2H]$^-$_1 determines the length of time the system was trapped as a peroxide adduct. This lifetime was less than 5 μs at low E_{col}, and was mostly spent on 5,8-OO-[G−H]$^-$. Consequently, no intermediates survived mass analysis.

To further explore the collision dynamics, we followed 100 trajectories for [G−H]$^-$ + $^1O_2$ at E_{col} = 0.1 eV, simulated at the B3LYP/6-31G level by using a direct dynamics method.[33] Of the trajectories, 35% belonged to direct, nonreactive collision (i.e., fly-by without forming complexes), and the remainder formed electrostatically bonded PC$^-$, some of which evolved to endoperoxide. However, upon termination of the trajectories (ca. 3 ps), most of the complex-forming trajectories decayed back to separated or loosely bonded reactant pairs. Less than 2% remained as the endoperoxide structure. It was not practical to propagate the trajectories long enough to exhaust all endoperoxides, but they were anticipated to eventually decay back to reactants on the basis of RRKM analysis.

One concern in the collisions of [G−H]$^-$ with $^1O_2$ is the possibility of electron transfer. The electron detachment energy for [G−H]$^-$ is 3.00 eV, calculated at the B3LYP/6-311++G** level. Assuming that the electronic excitation energy (0.98 eV)[34] and electron affinity (0.45 eV)[35] of O_2 could be used to drive electron transfer, this reaction is endothermic by 1.57 eV, and thus, could not occur in the E_{col} range of 0.1–1.0 eV.

3. Capturing endoperoxide formation in microhydrates

Both statistical modeling and dynamics simulations indicated that $^1O_2$ oxidation of gaseous [G+H]$^+$ and [G−H]$^-$ produced endoperoxides, yet these intermediates ultimately decomposed to starting reactants. This result reproduced the same instability problem, and thus, the failure of capturing endoperoxide in solution.[2a,11] To trap and measure endoperoxide in the gas phase, we had to figure out how to relax the initially excited intermediate. Such energy relaxation was realized in hydrated guanine ions because endoperoxides were indeed detected as end products in $^1O_2$ collisions with [G+H]$^+$(H_2O) and [G−H]$^-$(H_2O).

The oxidation product for the reaction of [G+H]$^+$(H_2O) (*m/z* 170) + $^1O_2$ was observed at *m/z* 184. This product channel can be attributed to liberation of a water ligand from a nascent hydrated endoperoxide. The reaction cross section is shown in Figure 4a, over the E_{col} range of 0.1 to 1.0 eV. The product mass spectrum taken at E_{col} = 0.1 eV is also shown in the inset of Figure 4a. A similar endoperoxide product channel was detected at *m/z* 182 for the reaction of [G−H]$^-$(H_2O) (*m/z* 168) + $^1O_2$. Its product mass spectrum and cross section are shown in Figure 4b.

The reaction cross sections for both [G+H]$^+$(H_2O) + $^1O_2$ and [G−H]$^-$(H_2O) + $^1O_2$ increase with decreasing E_{col}, which indicates that there are no activation barriers above the reactants. This observation is consistent with our calculated activation barriers for cycloaddition. These two systems have a similar reaction efficiency (ca. 2%) at the lowest E_{col} value, estimated from $\sigma_{reaction}/\sigma_{collision}$, in which $\sigma_{collision}$ is the greater of the ion-induced dipole capture cross section[36] and hard-sphere collision cross section. However, the efficiency for [G+H]$^+$(H_2O) drops more quickly than that of [G−H]$^-$(H_2O) in the high-energy regime.

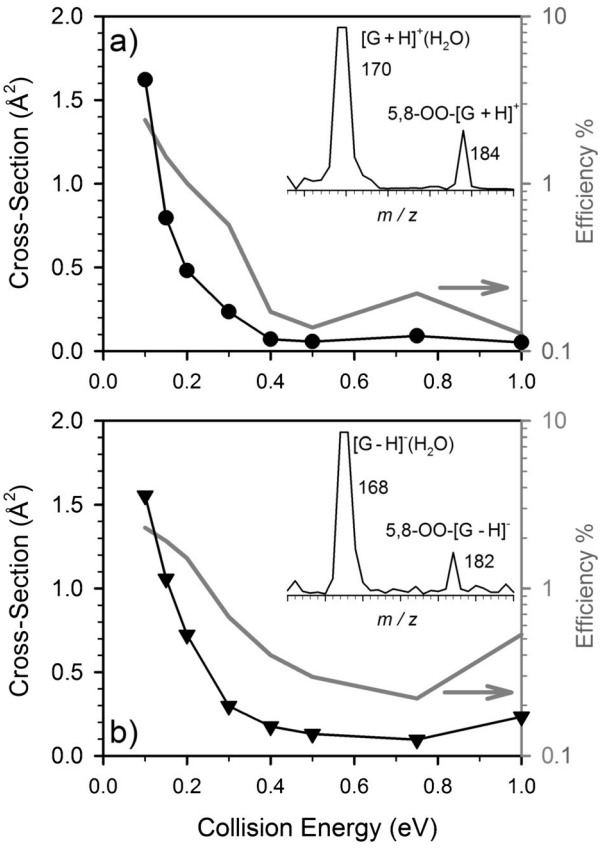

Figure 4. Reaction cross sections and efficiencies (dark gray lines against the right axis) for a) [G+H]$^+$(H_2O) + $^1O_2$ → 5,8-OO-[G+H]$^+$ + H_2O and b) [G−H]$^-$(H_2O) + $^1O_2$ → 5,8-OO-[G−H]$^-$ + H_2O. Insets show product mass spectra taken at E_{col} = 0.1 eV.

Relaxation of peroxide by water evaporation "cooling": The experimental results of hydrated guanine ions indicate that the oxidation of [G+H]$^+$ and [G−H]$^-$ is able to move on to stable products with the addition of a water ligand. First, let us look at the influence of microsolvation on the PES of [G+H]$^+$ + $^1O_2$, as illustrated in the inset of Figure 2. To differentiate between similar species in the dry and hydrated systems, we include a water ligand in the acronyms for the hydrated structures. Similar to that for [G+H]$^+$ + $^1O_2$, an energetically favorable pathway for the hydrated system corresponds to the formation of monohydrated 5,8-OO-[G+H]$^+$(H_2O). Except for the additional water ligand, the structures of the hydrated endoperoxide and the related TS are identical to those of their dehydrated analogues. The fate of the endoperoxide was, however, changed upon hydration. The driving force for this change came from the ejection of the water ligand from the hydrated endoperoxide. The water dissociation energy is 0.45 eV, which is below the dissociation threshold of the 5,8-OO-[G+H]$^+$ moiety. Water dissociation and accompanying product kinetic energy release efficiently removed the reaction heat of formation carried by nascent 5,8-OO-[G+H]$^+$, producing stable 5,8-OO-[G+H]$^+$ (ΔH_{rxn} = −0.07 eV). In this context, a single water

molecule resulted in a big change to the oxidation of $[G+H]^+$, and enabled capture of the otherwise unstable endoperoxide in the gas phase.

Compared with the protonated system, microsolvation had even more profound influences on the reaction of $[G-H]^- + {}^1O_2$. As shown in Figure 3b, water evaporation may lead to formation of three possible peroxides, as indicated by shaded arrows, which are 5,8-OO-$[G-H]^-$, 8-OOH$[G-2H]^-$, and 8-OOH$[G-2H]^-$_1, with $\Delta H_{rxn} = -0.69$, -1.80, and -1.09 eV, respectively. Albeit the least energetically favorable of the three structures, 5,8-OO-$[G-H]^-$ was verified as the most abundant product in trajectory simulations (see below), due to the least convoluted reaction path and lowest activation barrier. We also evaluated the possibility of losing water from 8-OO$[G-H]^-(H_2O)$; however, it was 0.1 eV endothermic and thus unlikely to compete with the other processes.

Dynamics insights from trajectory simulations: The water evaporation cooling mechanism was further supported by direct dynamics trajectory simulations. We integrated 200 trajectories for $[G-H]^-(H_2O) + {}^1O_2$ at $E_{col} = 0.1$ eV. Figure 5 exemplifies a representative scattering, resulting in 5,8-OO-$[G-H]^-$ and a separated water molecule. The top frame in Figure 5 shows the change in potential energy, the approach of reactants, and the separation of products (as indicated by the center-of-mass distances $r([G-H]^- - O_2)$ and $r([G-H]^- - H_2O)$) during the trajectory. The bottom frame in Figure 5 plots two new C–O bonds being formed in the endoperoxide. The trajectory verifies the reaction pathway proposed in Figure 3b. The formation of endoperoxide occurs at 1.5 ps, followed by repeated dissociation and reassociation of the endoperoxide bridge until water is eliminated at 5.8 ps. By the end of trajectory, water is separated from 5,8-OO-$[G-H]^-$ by 9 Å.

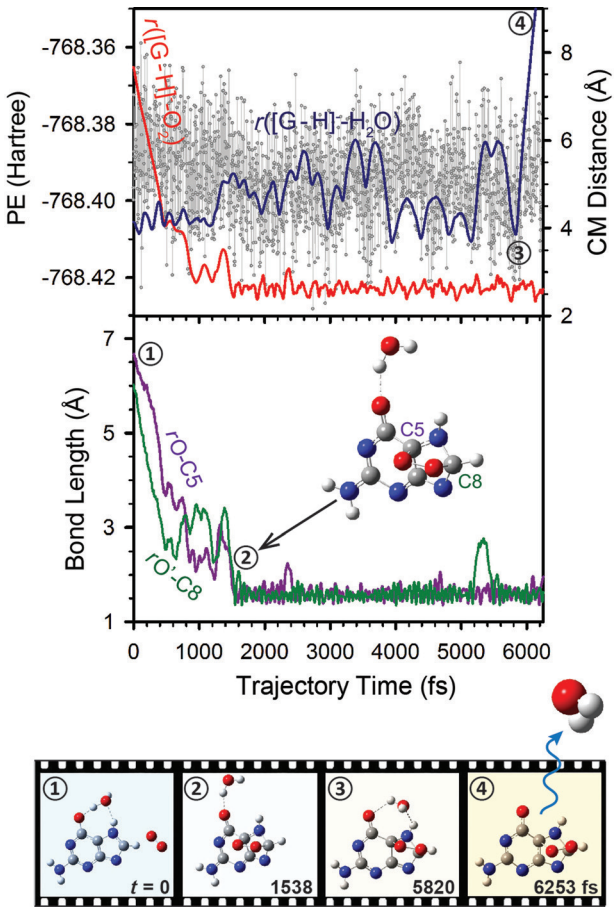

Figure 5. A representative trajectory shows the formation of 5,8-OO-$[G-H]^-$ in the collision of $[G-H]^-(H_2O) + {}^1O_2$ at $E_{col} = 0.1$ eV. A video of the trajectory is available in the Supporting Information.

Dynamics simulations show that, of the total 200 trajectories, more than 60% formed complexes, but most of these trajectories decayed back to reactants; only 5% remained as the endoperoxide structure until the end of the trajectories. The low branching ratio of reactive trajectories agrees with the low reaction efficiency measured in the ion-beam experiment.

One factor that may contribute to the low oxidation efficiency of guanine is that the water ligand may physically quench ${}^1O_2$. In the present experiment, we were not able to probe physical quenching of ${}^1O_2$, and the quasi-classical trajectories could not simulate the physical quenching of ${}^1O_2$. Viggiano et al. discovered that in the reaction of $OH^-(H_2O) + {}^1O_2$ excitation transfer-induced water dissociation followed a direct collision mechanism.[37] By assuming that similar direct excitation transfer-induced water dissociation occurred in the collision of $[G-H]^-(H_2O)$ with ${}^1O_2$, this would account for 22% of the trajectories in which ${}^1O_2$ attacked the water ligand directly.

In summary, the trajectory results verified complex mediation during guanine oxidation, identified the endoperoxide structure captured in the product mass spectra, and qualitatively reproduced the low reaction efficiency.

4. How closely does the gas-phase guanine mimic the oxidation of its nucleoside?

It is necessary to examine similarities and differences between the ${}^1O_2$ oxidation of free guanine and that of the guanosine nucleosides in DNA, so that we may extrapolate gas-phase findings to solution models. Scheme 1 outlines the oxidation products for dGuo $+ {}^1O_2$ in aqueous solution.[2a–j,l–s,26a] For clarity, we omitted products produced in low yields or those observed occasionally.[2k,n]

In contrast to gas-phase guanine, which has the predominant 7H-keto form, the guanosine moiety adopts the N9-substituted form, in which the N9 atom links to a sugar through a glycosidic bond. Consequently, different from guanine, which has the conjugated diene portion of the imidazole ring centered at C5=C4–N9=C8, dGuo has the corresponding conjugated center located at C4=C5–N7=C8. Cycloaddition of ${}^1O_2$ to dGuo occurs across C4–C8, leading to an endoperoxide, 4,8-OO-dGuo.[2a] The first step toward degradation of this highly active 4,8-OO-dGuo is rearrangement into 8-OOHdGuo. Subsequent loss of a water molecule from 8-OOHdGuo leads to an quinonoid intermediate, the C5=N7 bond of which is susceptible to nucleophilic attack.[2g–i,s] The addition of water to C5=N7 yields 5-OH-8-oxodGuo, the fate of which depends on the reaction pH and temperature. At low pH and temperature, 5-OH-

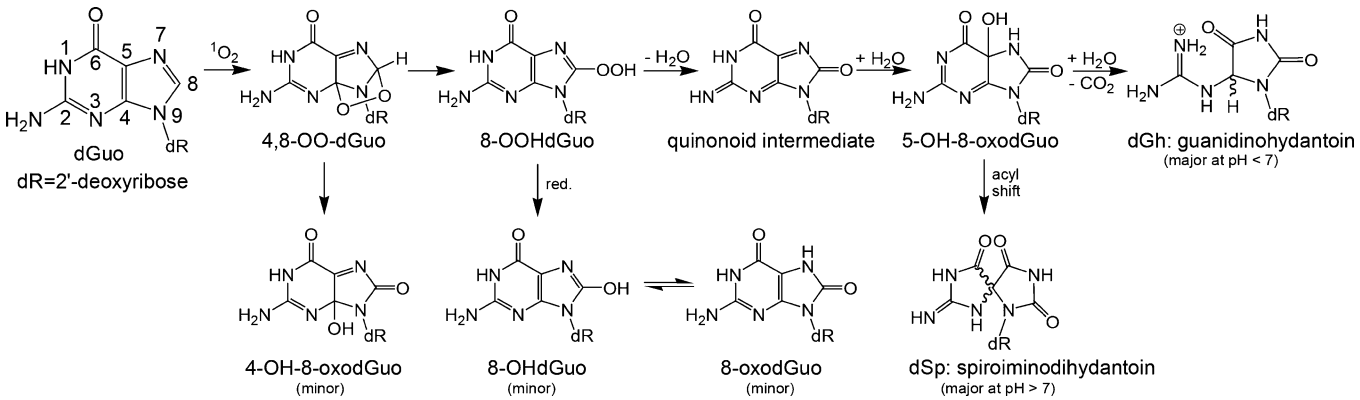

Scheme 1. The $^1O_2$-mediated oxidation paths and products of 2′-deoxyguanosine (dGuo) in aqueous solution.

oxodGuo hydrates, breaks C5–C6, and loses CO_2 to form dGh.[2g,26a] High pH and temperature, on the other hand, favor the rearrangement of 5-OH-oxodGuo into dSp through an acyl shift. The transformation of 5-OH-8-oxodGuo into dGh and dSp, as well as the interconversion between dSp and dGh, have been calculated by Burrows, Schlegel and co-workers.[26] In these reactions, explicit molecules of water are needed to complete hydrolysis and assist proton transfer. The formation of 8-oxodGuo represents a competitive reduction path of 8-OOH-dGuo, albeit minor.[2b,e] Another minor product is 4-OH-8-oxodGuo, which is formed by breaking the peroxide linkage.[2p]

To evaluate the resemblance between the oxidation of guanine and dGuo, we first explored the possibility of forming Gh- and Sp-like products in gas-phase $[G+H]^+ + {}^1O_2$. As shown in the PES of Figure 2, endoperoxide 5,8-OO-$[G+H]^+$ may break the peroxide linkage, leading to the formation of 5-OH-8-oxoG^+. As reported by Munk et al.[26b] (see Figure 4 in ref. [26b]), 5-OH-8-oxoG^+ may interconvert to protonated $[Gh+H]^+$. Figure 2 also suggests a route for the formation of protonated $[Sp+H]^+$ from 5-OH-8-oxoG^+. In contrast to the case of dGuo, no reactive or catalytic water is needed for the formation of $[Sp+H]^+$ from $[G+H]^+ + {}^1O_2$, although the system must cross barriers.

We were curious if deprotonated Sp and Gh could evolve in the oxidation of gas-phase $[G-H]^-$. No clear route was found leading to $[Gh-H]^-$ from deprotonated endoperoxide; this was not very surprising when considering the requirement of acidic conditions to produce dGh from dGuo. On the other hand, the formation of $[Sp-H]^-$ may be realized at high energies through the downstream product 8-oxo$[G-3H]^-$ formed from 5,8-OO-$[G-H]^-$. As illustrated in Figure 6, hydrolysis of 8-oxo$[G-3H]^-$ gives rise to 5-OH-8-oxo$[G-2H]^-$, and the latter interconverts into 5-O-8-oxo$[G-2H]^-$ through intramolecular proton transfer at TS3b$^-$. Finally, 5-O-8-oxo$[G-2H]^-$ evolves into $[Sp-H]^-$ through an acyl shift at TS3c$^-$. This process becomes feasible only in the presence of a reactive water molecule. Such a scenario is similar to the mechanism proposed for the oxidation of neutral guanosine by Burrows and co-workers.[2s]

Apart from Gh and Sp, the $^1O_2$ oxidation of gas-phase $[G+H]^+$ and $[G-H]^-$ leads to the formation of 8-oxo$[G-H]^+$, 5-OH-8-oxoG^+, and 8-oxo$[G-3H]^-$, which resemble the 8-oxodGuo and 4-OH-8-oxodGuo products shown in Scheme 1.

The major difference between guanine and guanosine arises from N9 substitution and the deprotonation sites. This difference is carried over into the structures of the corresponding endoperoxides, that is, 5,8-endoperoxide for guanine versus 4,8-endoperoxide for dGuo. Thus, the guanine model study mimicked some, but not all, of the reactivity of the guanosine nucleoside. 9-Methylguanine might be a better model compound, and a study of the $^1O_2$ reaction of protonated/deprotonated 9-methylguanine is currently underway.

Conclusion

The starting stage for singlet O_2 oxidation of the guanine nucleobase is believed to be the formation of an endoperoxide through a [4+2] cycloaddition. However, this transient endoperoxide is extremely unstable, and was only detected previously by low-temperature photosensitized oxidation of an 8-methyl-substituted guanosine derivative by NMR spectroscopy. We were able to capture peroxide intermediates in the collisions of gas-phase hydrated guanine ions (in both protonated and deprotonated states) with chemically generated singlet O_2 at room temperature by using guided-ion-beam mass spectrometry. Reaction PESs, kinetic modeling, and dynamics simulations strongly support a 5,8-endoperoxide structure. The successful capture of the 5,8-endoperoxide was due to relaxation of the excited intermediate product through water cluster dissociation. Possible pathways, leading from gas-phase endoperoxide to oxidation products Sp, Gh, and 8-oxoG, were discussed under conditions that mimicked acidic and basic solutions.

Experimental and Computational Section

Chemical generation of $^1O_2$

$^1O_2$ was generated by the reaction of $H_2O_2 + Cl_2 + 2KOH \rightarrow O_2$ (ca. 85% $X^3\Sigma_g^-$ and ca. 15% $a^1\Delta_g$) + 2KCl + $2H_2O$.[22] An 8 M solution of KOH (10.5 mL) was added to a 35 wt% aqueous solution of H_2O_2 (20 mL) in a sparger, which was immersed in a chiller at

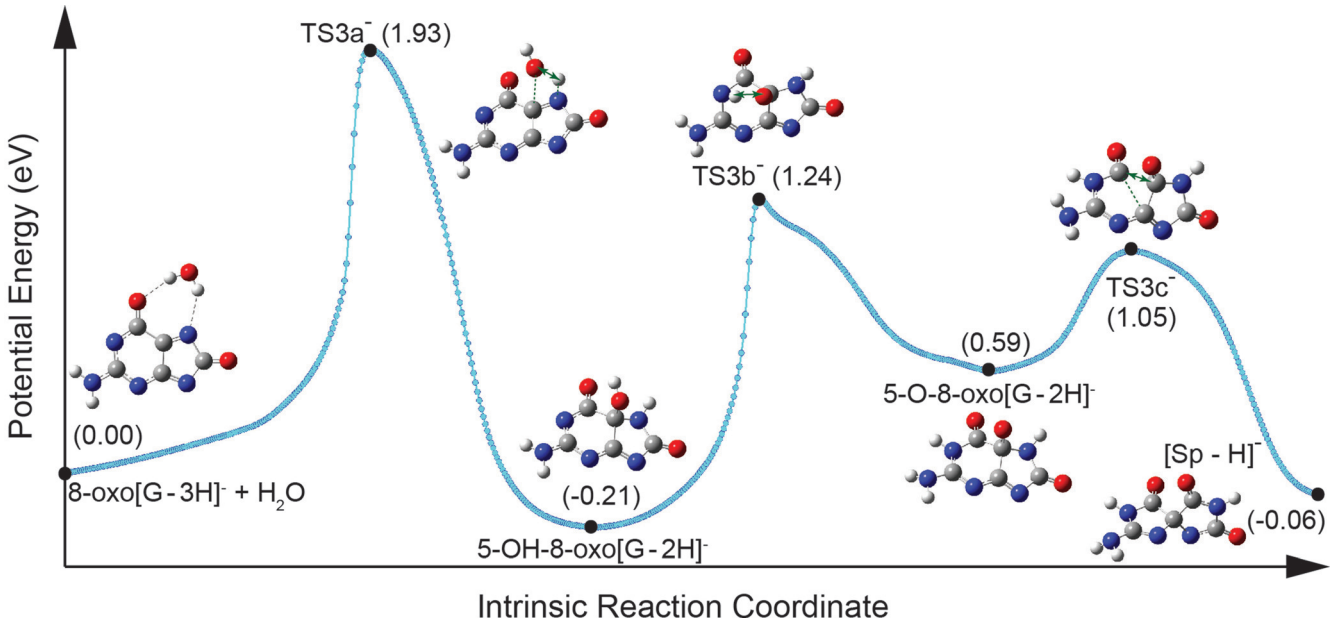

Figure 6. The PES for the water-assisted formation of $[Sp-H]^-$ from 8-oxo$[G-3H]^-$, constructed at the B3LYP/6-31+G* level, including thermal corrections at 298 K. A movie of the intrinsic reaction coordinate (IRC) trajectory is available in the Supporting Information.

−19 °C. The resulting mixture was degassed quickly. Cl_2 (3.4 sccm, ≥99.5%, Sigma–Aldrich) was mixed with He (53.5 sccm) and bubbled through the H_2O_2/KOH slush. All Cl_2 reacted with H_2O_2. Gaseous products were passed through a cold trap at −70 °C to remove water vapor. Only $^1O_2$, $^3O_2$, and He remained in the downstream gas.

Before leaking into the scattering cell of the mass spectrometer for ion–molecule reactions, the concentration of $^1O_2$ in the gas was determined by measuring the $^1O_2$ emission ($a^1\Delta_g \rightarrow X^3\Sigma_g^-$, $\nu = 0$–0)[34] at $\lambda = 1270$ nm in an optical emission cell. Emission from the cell was collected by using a plano-convex lens, passed through an optical chopper (SRS model SR540) and a 1270 nm interference filter, and focused into a thermoelectrically cooled InGaAs detector (Newport model 71887) coupled with a lock-in amplifier (SRS model SR830). Amplifier output was converted to absolute $^1O_2$ concentration based on a calibration.[38] To reduce the residence time, and therefore, the wall- and self-quenching of $^1O_2$, the entire $^1O_2$ generator was continuously pumped with a mechanical pump, and the pressure of the apparatus was maintained at 13 torr through a pressure relay (Cole–Parmer 00244OW). Pumping continuously replaced quenched O_2 with fresh $^1O_2$, so that a maximum $^1O_2$ concentration was available for ion–molecule reactions.

The $^1O_2$ generator also produced $^3O_2$. Fortunately, $^3O_2$ does not react with singlet closed-shell molecules because the reaction is spin-forbidden. To verify the nonreactivity of guanine ions toward $^3O_2$, control experiments were performed under the same conditions as those used for $^1O_2$, except that Cl_2 used in the $^1O_2$ generator was replaced by O_2 gas.

Gas-phase ion–molecule reactions

Reactions of protonated and deprotonated guanine ions with $^1O_2$ were carried out by using a homemade guided-ion-beam tandem mass spectrometer, which was described previously,[21] along with the operation, calibration, and data analysis procedures. The apparatus consisted of an ion source, radiofrequency (rf) hexapole ion guide, quadrupole mass filter, rf octopole ion guide surrounded by a scattering cell, second quadrupole mass filter, and a pulse-counting detector.

A sample solution for generating $[G+H]^+$ was prepared in HPLC-grade methanol/water (2:1 v/v) containing 0.05 mM guanine hydrochloride (99%, Alfa Aesar), and that for $[G-H]^-$ was prepared in methanol/water (3:1) containing 0.5 mM guanine (98%, Aldrich) and equimolar NaOH. The solution was sprayed into the ambient atmosphere through an electrospray needle at a flow rate of 0.05 mL h^{-1}. The ESI emitter was biased at 2.4 and −2.2 kV to produce positively and negatively charged species, respectively. Charged droplets entered the source chamber of the mass spectrometer through a desolvation capillary. The capillary was held at 100 V for positive ions and −90 V for negative ones, and the distance between the emitter tip and the entrance of the capillary was 1 cm. Liquid droplets underwent desolvation as they passed through the heated capillary, converting to gas-phase ions in the source chamber. Under mild heating conditions, not all of the solvent was evaporated, resulting in hydrated ions. In the experiment, the capillary was heated to 136–140 °C to optimize the intensities of dehydrated $[G+H]^+$ and $[G-H]^-$, and 112–115 °C for monohydrated $[G+H]^+(H_2O)$ and $[G-H]^-(H_2O)$. Increasing the ratio of water modestly in the ESI solution favored the intensities of monohydrates.

A skimmer with an orifice of 0.99 mm was located 3 mm from the capillary end, separating the source chamber and the hexapole ion guide. The skimmer was biased at 22 V for positive ions and −16 V for negative ones. Ions were transported into the hexapole at a pressure of 24 mTorr, and underwent collisional focusing and cooling to about 310 K. Ions subsequently passed into a conventional quadrupole for selection of specific reactant ions. Reactant ions were collected and focused into the octopole ion guide, which trapped ions in radical direction, minimizing loss of the reactant and product ions resulting from scattering. The octopole was surrounded by the scattering cell containing neutral reactant gas.

The cell pressure was measured by using a Baratron capacitance manometer (MKS 690 head and 670 signal conditioner).

After passing through the scattering cell, remaining reactant ions and product ions drifted to the end of the octopole, were mass analyzed by the second quadrupole, and counted. The initial kinetic energy distribution of the reactant ion beam was determined by using a retarding potential analysis,[39] that is, by measuring the intensity of the ion beam while scanning the direct current (DC) bias voltage applied to the octopole. The DC bias voltage also allowed control of the kinetic energy of reactant ions in the laboratory frame (E_{Lab}). E_{Lab} was converted into E_{col} between ions and $^1O_2$ molecules in the center-of-mass frame by using the equation $E_{col} = E_{Lab} \times m_{neutral}/(m_{ion}+m_{neutral})$, in which $m_{neutral}$ and m_{ion} were the masses of neutral and ionic reactants, respectively. The intensities of the reactant ion beam were 1×10^6 counts s^{-1} for dehydrated $[G+H]^+$ and $[G-H]^-$ and 2×10^5 counts s^{-1} for their monohydrates. Ion intensities were constant within 10% during the experiment. The initial kinetic energy of the ion beam was 0.9 to 1.1 eV, and the energy spread of the beam was 0.6 eV, which corresponded to 0.1 eV in the center-of-mass frame for the collisions of $[G+H]^+(H_2O)_{0,1}$/$[G-H]^-(H_2O)_{0,1}$ with $^1O_2$. Reaction cross sections were calculated from the ratios of reactant and product ion intensities (under single ion–molecule collision conditions), the pressure of $^1O_2$ in the scattering cell (= cell pressure × the fractional abundance of $^1O_2$), and the effective cell length. The scattering cell pressure was set at 0.25 mtorr, containing 5% of $^1O_2/^3O_2$ and 95% of He. Under these conditions, guanine ions underwent, at most, a single collision with O_2. Ions also collided with He, but the heavy-ion–light neutral molecule combination made these collisions insignificant at low E_{col}.

Electronic structure calculations, RRKM modeling, and dynamics simulations

Structures of reactants, intermediates, TSs, and products were optimized by using the Gaussian 09 program (rev. D.01).[40] The B3LYP/6-31+G*, B3LYP/6-311++G**, B3LYP/aug-cc-pVQZ, and CCSD(T)/6-31+G* levels of theory were used for most calculations. The single-reference-based methods were validated by running CASSCF and T1 diagnostics on critical reaction intermediates. The accuracy of the CCSD(T) and B3LYP energies were checked by using the MP3/aug-cc-pVTZ//MP2/6-31+G* results as a benchmark. The important structures along the most relevant reaction paths were also calculated at the wB97xD/6-31+G* level. The results from B3LYP and wB97xD functionals were in good agreement (see the Supporting Information), except that the energies of $TS2a^+$ and $TS2a^-$ in Figures 2 and 3 increased by about 0.4 eV at wB97xD; however, both B3LYP and wB97xD confirmed that $TS2a^+$ and $TS2a^-$ were mechanistically insignificant. Restricted–unrestricted instability was checked for the DFT calculations. For those without stable wave functions in restricted calculations, unrestricted DFT was performed and no spin contamination was found. Tautomer searching was conducted for all reactant ions, and their most stable tautomers were used as the starting structures in reaction coordinates, RRKM modeling, and trajectory simulations. All TSs were verified as first-order saddle points, and the vibrational mode with an imaginary frequency corresponded to the associated reaction pathway. IRC calculations were carried out for identified TS structures to make sure that the TSs were located between the correct energy minima. DFT-calculated vibrational frequencies and zero-point energies were scaled by a factor of 0.968 and 0.988,[41] respectively. Relative energies were obtained by including thermal corrections at 298 K. RRKM[31] rates were calculated with the program of Zhu and Hase[42] by using a direct state count algorithm and scaled DFT frequencies and energetics.

Direct dynamics simulations for the collisions of $[G-H]^-$ and $[G-H]^-(H_2O)$ with $^1O_2$ were carried out at $E_{col}=0.1$ eV by using Venus software[43] interfaced with the Gaussian 09 program. Due to the computational cost, a modest basis set was needed for a large set of dynamics trajectory simulations. To select a suitable level of theory, we performed relaxed PES scans for approach of $^1O_2$ to guanine ions in several orientations with various methods (including MP2/6-21G, MP2/6-31G, B3LYP/6-21G, B3LYP/6-31G, and B3LYP/6-31G*). We then compared these results to benchmark calculations consisting of single-point calculations at the geometries sampled in the relaxed PES scans at the B3LYP/6-311++G** and QCISD/cc-pVDZ levels of theory. Unfortunately, MP2 methods frequently ran into convergence failure. The PES shapes of the B3LYP methods with different basis sets were in reasonable agreement; the principle difference was that the well was slightly shallower when calculated with small basis sets. On the basis of the overall level of agreement and computational cost, we chose B3LYP/6-31G for trajectory integration. A small batch of reactive and nonreactive trajectories was repeated at the B3LYP/6-31+G* level. The difference between the trajectory outcomes with these two basis sets was below that of statistical uncertainty. Therefore, B3LYP/6-31G was expected to reasonably describe the gross dynamics feature of $^1O_2$ attack.

The initial separation between collision partners was set at 8.0 Å (at which the attractive potential between reactants was only a few meV), with a collision impact parameter of 0 Å. The vibrational and rotational temperatures of all reactants were set at 300 K, which were chosen to mimic the ion–molecule experiment. Quasi-classical Boltzmann sampling[44] was used to select vibrational and rotational energies.

The Hessian-based predictor–corrector algorithm[33b] was used for numerical integration of the classical equations of motion, with the Hessian matrix being updated every five steps. A step size of 0.25 $amu^{1/2}$ Bohr (corresponding to a step size of 0.5–0.6 fs in trajectory time) was used for trajectories. The initial guess of molecular orbital for each DFT calculation was obtained from the previous step, and the total energy of the system was checked during the simulation to ensure that the energy was conserved to better than 10^{-4} hartree. The SCF=XQC option was adopted for the trajectory integration, so that a quadratically convergent SCF method was used in case the conventional first-order SCF algorithm failed to converge within allotted cycles. Trajectories were terminated when the product separation exceeded 8.1 Å. A total of 300 trajectories were accomplished in the work, each taking about 340 cpu hours on an Intel 12 core based computational cluster. gOpenMol[45] was used for trajectory visualization. Analysis of individual trajectories and statistical analysis of the trajectory ensemble were performed by using programs written for these purposes.

Acknowledgements

This work was supported by Grants from the National Science Foundation (CHE 0954507 and 1464171) and PSC-CUNY Research Award. W.L. was the recipient of the CUNY Doctoral Student Research Grant in 2015.

Keywords: density functional calculations · ion–molecule reactions · mass spectrometry · molecular dynamics · singlet oxygen

[1] D. T. Sawyer, *Oxygen Chemistry*, Oxford University Press, New York, **1991**.
[2] a) C. Sheu, C. S. Foote, *J. Am. Chem. Soc.* **1993**, *115*, 10446 – 10447; b) J. Cadet, T. Douki, J.-P. Pouget, J.-L. Ravanat, *Methods Enzymol.* **2000**, *319*, 143 – 153; c) J.-L. Ravanat, P. Di Mascio, G. R. Martinez, M. H. G. Medeiros, J. Cadet, *J. Biol. Chem.* **2000**, *275*, 40601 – 40604; d) J.-L. Ravanat, T. Douki, J. Cadet, *J. Photochem. Photobiol. B* **2001**, *63*, 88 – 102; e) J.-L. Ravanat, C. Saint-Pierre, P. Di Mascio, G. R. Martinez, M. H. G. Medeiros, J. Cadet, *Helv. Chim. Acta* **2001**, *84*, 3702 – 3709; f) J. C. Niles, J. S. Wishnok, S. R. Tannenbaum, *Org. Lett.* **2001**, *3*, 963 – 966; g) Y. Ye, J. G. Muller, W. Luo, C. L. Mayne, A. J. Shallop, R. A. Jones, C. J. Burrows, *J. Am. Chem. Soc.* **2003**, *125*, 13926 – 13927; h) J.-L. Ravanat, G. R. Martinez, M. H. G. Medeiros, P. D. Mascio, J. Cadeta, *Arch. Biochem. Biophys.* **2004**, *423*, 23 – 30; i) M. E. Hosford, J. G. Muller, C. J. Burrows, *J. Am. Chem. Soc.* **2004**, *126*, 9540 – 9541; j) J. E. B. McCallum, C. Y. Kuniyoshi, C. S. Foote, *J. Am. Chem. Soc.* **2004**, *126*, 16777 – 16782; k) M. R. Iesce, F. Cermola, F. Temussi, *Current Organic Chemistry* **2005**, *9*, 109 – 139; l) J. Cadet, S. Courdavault, J.-L. Ravanat, T. Douki, *Pure Appl. Chem.* **2009**, *77*, 947 – 961; m) J. Cadet, J.-L. Ravanat, G. R. Martinez, M. H. G. Medeiros, P. D. Mascio, *Photochem. Photobiol.* **2006**, *82*, 1219 – 1225; n) T. Gimisis, C. Cismas, *Eur. J. Org. Chem.* **2006**, 1351 – 1378; o) W. L. Neeley, J. M. Essigmann, *Chem. Res. Toxicol.* **2006**, *19*, 491 – 505; p) J.-L. Ravanat, G. R. Martinez, M. H. G. Medeiros, P. Di Mascio, J. Cadet, *Tetrahedron* **2006**, *62*, 10709 – 10715; q) J. Cadet, T. Douki, J.-L. Ravanat, *Acc. Chem. Res.* **2008**, *41*, 1075 – 1083; r) M. Zamadar, A. Greer in *Handbook of Synthetic Photochemistry* (Eds.: A. Albini, M. Fagnoni), Wiley-VCH, Weinheim, **2010**, pp. 353 – 386; s) A. M. Fleming, E. I. Armentrout, J. Zhu, J. G. Muller, C. J. Burrows, *J. Org. Chem.* **2015**, *80*, 711 – 721.
[3] a) V. Duarte, D. Gasparutto, L. F. Yamaguchi, J.-L. Ravanat, G. R. Martinez, M. H. G. Medeiros, P. D. Mascio, J. Cadet, *J. Am. Chem. Soc.* **2000**, *122*, 12622 – 12628; b) J. Cadet, P. D. Mascio in *Modified Nucleosides: in Biochemistry Biotechnology and Medicine* (Ed.: P. Herdewijn), Wiley-VCH, Weinheim, **2008**.
[4] a) L. J. Marnett, P. C. Burcham, *Chem. Res. Toxicol.* **1993**, *6*, 771 – 785; b) C. J. Burrows, J. G. Muller, *Chem. Rev.* **1998**, *98*, 1109 – 1151; c) B. Armitage, *Chem. Rev.* **1998**, *98*, 1171 – 1200.
[5] S. D. Bruner, D. P. G. Norman, G. L. Verdine, *Nature* **2000**, *403*, 859 – 866.
[6] P. T. Henderson, J. C. Delaney, J. G. Muller, W. L. Neeley, S. R. Tannenbaum, C. J. Burrows, J. M. Essigmann, *Biochemistry* **2003**, *42*, 9257 – 9262.
[7] a) M. A. Lovell, W. R. Markesbery, *Arch. Neurol.* **2001**, *58*, 392 – 396; b) J. Zhang, G. Perry, M. A. Smith, D. Robertson, S. J. Olson, D. G. Graham, T. J. Montine, *Am. J. Pathol.* **1999**, *154*, 1423 – 1429.
[8] X. Xu, J. G. Muller, Y. Ye, C. J. Burrows, *J. Am. Chem. Soc.* **2008**, *130*, 703 – 709.
[9] C. S. Foote, *Science* **1968**, *162*, 963 – 970.
[10] G. R. Martinez, J.-L. Ravanat, M. H. G. Medeiros, J. Cadet, P. Di Mascio, *J. Am. Chem. Soc.* **2000**, *122*, 10212 – 10213.
[11] a) P. Kang, C. S. Foote, *J. Am. Chem. Soc.* **2002**, *124*, 4865 – 4873; b) C. Sheu, P. Kang, S. Khan, C. S. Foote, *J. Am. Chem. Soc.* **2002**, *124*, 3905 – 3913.
[12] a) H. H. Seliger, *Anal. Biochem.* **1960**, *1*, 60 – 65; b) A. Khan, M. Kasha, *J. Chem. Phys.* **1963**, *39*, 2105 – 2106.
[13] P. B. Armentrout, *J. Anal. At. Spectrom.* **2004**, *19*, 571 – 580.
[14] a) M. T. Rodgers, S. Campbell, E. M. Marzluff, J. L. Beauchamp, *Int. J. Mass Spectrom. Ion Processes* **1994**, *137*, 121 – 149; b) M. T. Rodgers, P. B. Armentrout, *J. Am. Chem. Soc.* **2002**, *124*, 2678 – 2691; c) Z. Yang, M. T. Rodgers, *Phys. Chem. Chem. Phys.* **2004**, *6*, 2749 – 2757; d) Y. W. Nei, T. E. Akinyemi, J. D. Steill, J. Oomens, M. T. Rodgers, *Int. J. Mass Spectrom.* **2010**, *297*, 139 – 151; e) Y. W. Nei, T. E. Akinyemi, C. M. Kaczan, J. D. Steill, G. Berden, J. Oomens, M. T. Rodgers, *Int. J. Mass Spectrom.* **2011**, *308*, 191 – 202; f) Z. Yang, M. T. Rodgers, *Phys. Chem. Chem. Phys.* **2012**, *14*, 4517 – 4526; g) Y. W. Nei, K. T. Crampton, G. Berden, J. Oomens, M. T. Rodgers, *J. Phys. Chem. A* **2013**, *117*, 10634 – 10649; h) Y. W. Nei, N. Hallowita, J. D. Steill, J. Oomens, M. T. Rodgers, *J. Phys. Chem. A* **2013**, *117*, 1319 – 1335; i) B. Yang, R. R. Wu, G. Berden, J. Oomens, M. T. Rodgers, *J. Phys. Chem. B* **2013**, *117*, 14191 – 14201; j) B. Yang, R. R. Wu, N. C. Polfer, G. Berden, J. Oomens, M. T. Rodgers, *J. Am. Soc. Mass Spectrom.* **2013**, *24*, 1523 – 1533; k) B. Yang, R. R. Wu, M. T. Rodgers, *Anal. Chem.* **2013**, *85*, 11000 – 11006; l) B. Yang, M. T. Rodgers, *Phys. Chem. Chem. Phys.* **2014**, *16*, 16110 – 16120; m) B. Yang, M. T. Rodgers, *J. Am. Chem. Soc.* **2014**, *136*, 282 – 290; n) J. M. Gregson, J. A. McCloskey, *Int. J. Mass Spectrom. Ion Proc.* **1997**, *165/166*, 475 – 485; o) M. A. Freitas, S. D. H. Shi, C. L. Hendrickson, A. G. Marshall, *J. Am. Chem. Soc.* **1998**, *120*, 10187 – 10193; p) R. Tuytten, F. Lemière, E. L. Esmans, W. A. Herrebout, B. J. v. d. Veken, E. Dudley, R. P. Newton, E. Witters, *J. Am. Soc. Mass Spectrom.* **2006**, *17*, 1050 – 1062; q) R. Wu, T. B. McMahon, *J. Am. Chem. Soc.* **2007**, *129*, 569 – 580; r) J. Sultan, *Int. J. Mass Spectrom.* **2008**, *273*, 58 – 68; s) Y. Seong, S. Y. Han, S.-C. Jo, H. B. Oh, *Mass Spectrom. Lett.* **2011**, *2*, 73 – 75.
[15] a) J. Lin, C. Yu, S. Peng, I. Akiyama, K. Li, L. K. Lee, P. R. LeBreton, *J. Phys. Chem.* **1980**, *84*, 1006 – 1012; b) E. Nir, L. Grace, B. Brauer, M. S. de Vries, *J. Am. Chem. Soc.* **1999**, *121*, 4896 – 4897; c) E. Nir, C. Janzen, P. Imhof, K. Kleinermanns, M. S. de Vries, *J. Chem. Phys.* **2001**, *115*, 4604 – 4611; d) F. Piuzzi, M. Mons, I. Dimicoli, B. Tardivel, Q. Zhao, *Chem. Phys.* **2001**, *270*, 205 – 214; e) M. Mons, I. Dimicoli, F. Piuzzi, B. Tardivel, M. Elhanine, *J. Phys. Chem. A* **2002**, *106*, 5088 – 5094; f) C. Colominas, F. J. Luque, M. Orozco, *J. Am. Chem. Soc.* **1996**, *118*, 6811 – 6821; g) Y. Podolyan, L. Gorb, J. Leszczynski, *J. Phys. Chem. A* **2000**, *104*, 7346 – 7352; h) B. Mennucci, A. Toniolo, J. Tomasi, *J. Phys. Chem. A* **2001**, *105*, 7126 – 7134; i) M. Hanus, F. Ryjáček, M. Kabeláč, T. Kubař, T. V. Bogdan, S. A. Trygubenko, P. Hobza, *J. Am. Chem. Soc.* **2003**, *125*, 7678 – 7688; j) Y. H. Jang, W. A. G. II, K. T. Noyes, L. C. Sowers, S. Hwang, D. S. Chung, *J. Phys. Chem. B* **2003**, *107*, 344 – 357; k) W. Liang, H. Li, X. Hu, S. Han, *Chem. Phys.* **2006**, *328*, 93 – 102.
[16] a) N. Russo, M. Toscano, A. Grand, F. Jolibois, *J. Comput. Chem.* **1998**, *19*, 989 – 1000; b) A. K. Chandra, M. T. Nguyen, T. Uchimaru, T. Zeegers-Huyskens, *J. Phys. Chem. A* **1999**, *103*, 8853 – 8860; c) B. Giese, D. McNaughton, *Phys. Chem. Chem. Phys.* **2002**, *4*, 5161 – 5170; d) J. D. Zhang, Y. Xie, H. F. Schaefer III, *J. Phys. Chem. A* **2006**, *110*, 12010 – 12016.
[17] F. Greco, A. Liguori, G. Sindona, N. Uccella, *J. Am. Chem. Soc.* **1990**, *112*, 9092 – 9096.
[18] E. P. Hunter, S. G. Lias, *J. Phys. Chem. Ref. Data* **1998**, *27*, 413 – 656.
[19] a) E. C. M. Chen, C. Herder, E. S. Chen, *J. Mol. Struct.* **2006**, *798*, 126 – 133; b) Y. Huang, H. Kenttamaa, *J. Phys. Chem. A* **2004**, *108*, 4485 – 4490.
[20] a) A. K. Chandra, M. T. Nguyen, T. Uchimaru, T. Zeegers-Huyskens, *J. Mol. Struct.* **2000**, *555*, 61 – 66; b) O. V. Shishkin, O. S. Sukhanov, L. Gorb, J. Leszczynski, *Phys. Chem. Chem. Phys.* **2002**, *4*, 5359 – 5364.
[21] Y. Fang, J. Liu, *J. Phys. Chem. A* **2009**, *113*, 11250 – 11261.
[22] a) A. Midey, I. Dotan, A. A. Viggiano, *J. Phys. Chem. A* **2008**, *112*, 3040 – 3045; b) Y. Fang, F. Liu, A. Bennett, S. Ara, J. Liu, *J. Phys. Chem. B* **2011**, *115*, 2671 – 2682.
[23] A. M. Kamel, B. Munson, *Eur. J. Mass Spectrom.* **2004**, *10*, 239 – 257.
[24] C. A. Cole, Z.-C. Wang, T. P. Snow, V. M. Bierbaum, *J. Phys. Chem. A* **2015**, *119*, 334 – 343.
[25] X. Zou, H. Zhao, Y. Yu, H. Su, *J. Am. Chem. Soc.* **2013**, *135*, 4509 – 4515.
[26] a) Y. Ye, B. H. Munk, J. G. Muller, A. Cogbill, C. J. Burrows, H. B. Schlegel, *Chem. Res. Toxicol.* **2009**, *22*, 526 – 535; b) B. H. Munk, C. J. Burrows, H. B. Schlegel, *J. Am. Chem. Soc.* **2008**, *130*, 5245 – 5256.
[27] J. Méndez-Hurtado, R. López, D. Suárez, M. I. Menéndez, *Eur. J. Chem.* **2012**, *18*, 8437 – 8447.
[28] M. Bobrowski, A. Liwo, S. Oldziej, D. Jeziorek, T. Ossowski, *J. Am. Chem. Soc.* **2000**, *122*, 8112 – 8119.
[29] R. Grüber, A. Monari, E. Dumont, *J. Phys. Chem. A* **2014**, *118*, 11612 – 11619.
[30] W. M. Luo, J. G. Muller, E. M. Rachlin, C. J. Burrows, *Org. Lett.* **2000**, *2*, 613 – 616.
[31] R. A. Marcus, *J. Chem. Phys.* **1952**, *20*, 359 – 364.
[32] L. Zhu, W. L. Hase, *Chem. Phys. Lett.* **1990**, *175*, 117 – 124.
[33] a) K. Bolton, W. L. Hase in *Modern Methods for Multidimensional Dynamics Computations in Chemistry*, (Ed: D. L. Thompson), World Scientific, Singapore, **1998**, pp. 143 – 189; b) V. Bakken, J. M. Millam, H. B. Schlegel, *J. Chem. Phys.* **1999**, *111*, 8773 – 8777.
[34] W. J. Lafferty, A. M. Solodov, C. L. Lugez, G. T. Fraser, *Appl. Opt.* **1998**, *37*, 2264 – 2270.
[35] K. M. Ervin, I. Anusiewicz, P. Skurski, J. Simons, W. C. Lineberger, *J. Phys. Chem. A* **2003**, *107*, 8521 – 8529.
[36] J. Troe, *Chem. Phys. Lett.* **1985**, *122*, 425 – 430.
[37] A. A. Viggiano, A. Midey, N. Eyet, V. M. Bierbaum, J. Troe, *J. Chem. Phys.* **2009**, *131*, 094303.
[38] F. Liu, Y. Fang, Y. Chen, J. Liu, *J. Phys. Chem. B* **2012**, *116*, 6369 – 6379.
[39] K. M. Ervin, P. B. Armentrout, *J. Chem. Phys.* **1985**, *83*, 166 – 189.

[40] Gaussian 09, Revision D.01, M. J. Frisch, G. W. Trucks, H. B. Schlegel, G. E. Scuseria, M. A. Robb, J. R. Cheeseman, G. Scalmani, V. Barone, B. Mennucci, G. A. Petersson, H. Nakatsuji, M. Caricato, X. Li, H. P. Hratchian, A. F. Izmaylov, J. Bloino, G. Zheng, J. L. Sonnenberg, M. Hada, M. Ehara, K. Toyota, R. Fukuda, J. Hasegawa, M. Ishida, T. Nakajima, Y. Honda, O. Kitao, H. Nakai, T. Vreven, J. J. A. Montgomery, J. E. Peralta, F. Ogliaro, M. Bearpark, J. J. Heyd, E. Brothers, K. N. Kudin, V. N. Staroverov, T. Keith, R. Kobayashi, J. Normand, K. Raghavachari, A. Rendell, J. C. Burant, S. S. Iyengar, J. Tomasi, M. Cossi, N. Rega, J. M. Millam, M. Klene, J. E. Knox, J. B. Cross, V. Bakken, C. Adamo, J. Jaramillo, R. Gomperts, R. E. Stratmann, O. Yazyev, A. J. Austin, R. Cammi, C. Pomelli, J. W. Ochterski, R. L. Martin, K. Morokuma, V. G. Zakrzewski, G. A. Voth, P. Salvador, J. J. Dannenberg, S. Dapprich, A. D. Daniels, O. Farkas, J. B. Foresman, J. V. Ortiz, J. Cioslowski, D. J. Fox, Wallingford, CT, **2013**.

[41] M. P. Andersson, P. Uvdal, *J. Phys. Chem. A* **2005**, *109*, 2937 – 2941.

[42] L. Zhu, W. L. Hase, Chemistry Department, University of Indiana, Bloomington, **1993**.

[43] W. L. Hase, K. Bolton, P. de Sainte Claire, R. J. Duchovic, X. Hu, A. Komornicki, G. Li, K. Lim, D. Lu, G. H. Peslherbe, K. Song, K. N. Swamy, S. R. Vande Linde, A. Varandas, H. Wang, R. J. Wolf, Texas Tech Univeristy Lubbock, TX, **1999**.

[44] G. H. Peslherbe, H. Wang, W. L. Hase, *Adv. Chem. Phys.* **1999**, *105*, 177 – 201.

[45] L. Laaksonen, 3.0 ed., Center for Scientific Computing, Espoo, Finland, **2005**, p. available at www.csc.fi/gopenmol/.

Received: October 14, 2015
Published online on January 27, 2016

